Atmos. Chem. Phys. Discuss., https://doi.org/10.5194/acp-2018-480
Manuscript under review for journal Atmos. Chem. Phys.
Discussion started: 13 June 2018
© Author(s) 2018. CC BY 4.0 License.

Atmospheric Chemistry and Physics
Discussions

Turbulent enhancement of radar reflectivity factor for polydisperse cloud droplets

Keigo Matsuda[1] and Ryo Onishi[1]

[1]Center for Earth Information Science and Technology (CEIST), Japan Agency for Marine-Earth Science and Technology (JAMSTEC), 3173-25 Showa-machi, Kanazawa-ku, Yokohama 236-0001, Japan

Correspondence to: Keigo Matsuda (k.matsuda@jamstec.go.jp)

Abstract. The radar reflectivity factor is important for estimating cloud microphysical properties; thus, in this study, we determine the quantitative influence of microscale turbulent clustering of polydisperse droplets on the radar reflectivity factor. The theoretical solution for particulate Bragg scattering is obtained without assuming monodisperse droplet sizes. The scattering intensity is given by an integral function including the cross spectrum of number density fluctuations for two different droplet sizes. We calculate the cross spectrum based on turbulent clustering data, which are obtained by the direct numerical simulation (DNS) of particle-laden homogeneous isotropic turbulence. The results show that the coherence of the cross spectrum is close to unity for small wavenumbers and decreases almost exponentially with increasing wavenumber. This decreasing trend is dependent on the combination of Stokes numbers. A critical wavenumber is introduced to characterize the exponential decrease of the coherence and parametrized using the Stokes number difference. Comparison with DNS results confirms that the proposed model can reproduce the r_p^3-weighted power spectrum, which is proportional to the clustering influence on the radar reflectivity factor, to a sufficiently high accuracy. The model is then applied to high-resolution cloud-simulation data obtained from a spectral-bin cloud simulation. The result shows that the influence of turbulent clustering can be significant for the near-top of turbulent clouds.

1 Introduction

Radar remote sensing is widely used for observing a spatial distribution of cloud and precipitation particles because it can also provide estimates of cloud microphysical properties. The remote sensing data are analyzed and displayed using the radar reflectivity factor (mm^6 m^{-3}), Z, which is obtained by the following radar equation:

$$P_\mathrm{r} = \frac{P_\mathrm{t} G A_\mathrm{e} k_\mathrm{m}^4 |K|^2 V}{4^4 R^4} Z, \tag{1}$$

where P_r and P_t are the received and transmitted microwave powers, respectively, G is the antenna gain, A_e is the effective aperture of the antenna, k_m is the microwave wavenumber, K is the dielectric coefficient of a water droplet, V is the measurement volume, and R is the distance between the antenna and the cloud. The relationship between the radar reflectivity factor and cloud microphysical properties is usually expressed based on the assumption of incoherent scattering (Gossard and Strauch, 1983). Incoherent scattering implies random and uniform dispersion of cloud droplets (Bohren and Huffman, 1983).

Atmos. Chem. Phys. Discuss., https://doi.org/10.5194/acp-2018-480
Manuscript under review for journal Atmos. Chem. Phys.
Discussion started: 13 June 2018
© Author(s) 2018. CC BY 4.0 License.

Atmospheric Chemistry and Physics
Open Access
Discussions

For this case, the factor is proportional to the sum of the scattering intensities of the individual droplets in the measurement volume. In contrast, droplets form a nonuniform spatial distribution in turbulence, i.e. inertial particles concentrate in small-enstrophy regions during turbulence due to the centrifugal motion (Maxey, 1987; Squires and Eaton, 1991; Wang and Maxey, 1993; Chen et al., 2006). This preferential concentration is often referred to as turbulent clustering. Nonuniform distribution of cloud droplets results in coherent scattering, which is also referred to as particulate Bragg scattering (Kostinski and Jameson, 2000). For this case, the interference of microwaves scattered by nonuniformly distributed droplets increases the scattered microwave intensity; i.e., the radar reflectivity factor increases due to particulate Bragg scattering. The radar reflectivity factor for particulate Bragg scattering is dependent on the microwave frequency $f_{\rm m}$ ($= k_{\rm m}c/2\pi$, where c is the speed of light), while the factor for incoherent scattering is independent of $f_{\rm m}$. Knight and Miller (1998) and Rogers and Brown (1997) reported radar frequency dependence of their observation results, and Kostinski and Jameson (2000) pointed out the possibility that particulate Bragg scattering due to turbulent clustering leads to frequency dependence. To evaluate the quantitative influence of turbulent clustering on the radar reflectivity factor, it is crucial to understand the spatial structure of turbulent clustering. Turbulent clustering has been discussed in many literatures because it can enhance the collision growth of cloud droplets (e.g., Sundaram and Collins, 1997; Reade and Collins, 2000; Ayala et al., 2008a, b; Onishi et al., 2009; Wang et al., 2009; Onishi and Vassilicos, 2014), and statistical data on turbulent clustering have been obtained for scales relevant to droplet collisions. However, these data cannot be adopted for particulate Bragg scattering because the clustering scales relevant to particulate Bragg scattering are on the microwave wavelength, which is larger than droplet collision scales. Quantitative estimate of particulate Bragg scattering due to turbulent clustering is first provided by Dombrovsky and Zaichik (2010). Their analytical estimate was based on a clustering model for droplet collision scales but indicated that turbulent clustering can lead to considerable increase in the radar reflectivity factor. Matsuda et al. (2014) clarified the quantitative influence based on turbulent clustering data obtained by a three-dimensional direct numerical simulation (DNS), which covered the clustering scales on the microwave wavelength. They estimated the increase in the radar reflectivity factor due to turbulent clustering by calculating the power spectrum of number density fluctuations $E_{\rm np}(k|r_{\rm p})$, where k is the wavenumber and $r_{\rm p}$ is the droplet radius. The power spectrum $E_{\rm np}(k|r_{\rm p})$ is strongly dependent on the droplet size: More specifically, $E_{\rm np}(k|r_{\rm p})$ is dependent on the Stokes number, St, which is defined as ${\rm St} \equiv \tau_{\rm p}/\tau_\eta$ ($\tau_{\rm p}$ is the relaxation time of droplet motion and τ_η is the Kolmogorov time). However, the discussion of radar reflectivity factor increases is limited to cases of monodisperse particles. Thus, the results are not directly applicable to particulate Bragg scattering for real cloud systems, in which cloud droplets have broad droplet size distributions.

Therefore, this study aims to investigate the influence of turbulent clustering of polydisperse droplets on particulate Bragg scattering. Firstly, the theoretical formulation of particulate Bragg scattering is extended for polydisperse particles and expressed using the cross spectrum of number density fluctuations for two different droplet sizes. Secondly, the three-dimensional DNS of particle-laden homogeneous isotropic turbulence is performed to obtain turbulent droplet clustering data, which are used to calculate the power spectrum and the cross spectrum of number density fluctuations. An empirical parameterization for the cross spectrum is then proposed considering the dependence of the Stokes number combination. Finally, in order to investigate the impact of turbulent clustering on radar observations of realistic clouds, the proposed model is applied to high-resolution cloud-simulation data obtained by a spectral-bin cloud microphysics simulation.

Atmos. Chem. Phys. Discuss., https://doi.org/10.5194/acp-2018-480
Manuscript under review for journal Atmos. Chem. Phys.
Discussion started: 13 June 2018
© Author(s) 2018. CC BY 4.0 License.

2 Theory

Here, we aim to formulate the radar reflectivity factor Z for a nonuniform distribution of polydisperse cloud droplets based on the discussion of Gossard and Strauch (1983), but without assuming monodisperse droplet sizes. Because the radii of cloud droplets are much smaller than the microwave wavelength, the electric field vector of the microwaves scattered by a single droplet, $\mathbf{E}_{\rm sca}(t,\mathbf{x},r_{\rm p})$, is given by the Rayleigh scattering approximation:

$$\mathbf{E}_{\rm sca}(t,\mathbf{x},r_{\rm p}) = \mathbf{E}_{\rm inc}\frac{k_{\rm m}^2 K r_{\rm p}^3}{R}\sin\chi\exp\left[i\left\{\omega t - \mathbf{k}_{\rm sca}\cdot(\mathbf{x}_{\rm r}-\mathbf{x}) - \mathbf{k}_{\rm inc}\cdot(\mathbf{x}-\mathbf{x}_{\rm t})\right\}\right], \quad (2)$$

where $\mathbf{E}_{\rm inc}$ is the electric field amplitude vector of the incident microwave, $r_{\rm p}$ is the droplet radius, $\mathbf{x}$, $\mathbf{x}_{\rm t}$, and $\mathbf{x}_{\rm r}$ are the position vectors of the droplet, microwave transmitter, and microwave receiver, respectively, $\mathbf{k}_{\rm inc}$ and $\mathbf{k}_{\rm sca}$ are the wavenumber vectors of the incident and scattered microwaves, respectively, which satisfy $|\mathbf{k}_{\rm inc}| = |\mathbf{k}_{\rm sca}| = k_{\rm m}$, and χ is the angle between $\mathbf{E}_{\rm inc}$ and $\mathbf{k}_{\rm sca}$. Considering the droplet-size dependence of $\mathbf{E}_{\rm sca}(t,\mathbf{x},r_{\rm p})$, the electric power of the microwave scattered by a group of droplets, $P_{\rm s}$, is given by

$$P_{\rm s} = \overline{\left|\int_{\mathbf{x}\in V}\int_0^\infty \mathbf{E}_{\rm sca}(t,\mathbf{x},r_{\rm p})n(\mathbf{x},r_{\rm p})dr_{\rm p}d\mathbf{x}\right|^2}/\zeta, \quad (3)$$

where $n(\mathbf{x},r_{\rm p})dr_{\rm p}d\mathbf{x}$ is the number of droplets with radii from $r_{\rm p}$ to $r_{\rm p}+dr_{\rm p}$ in an infinitesimal volume $d\mathbf{x}$ at position $\mathbf{x}$, and ζ is the intrinsic impedance. The overbar denotes the temporal average. The relationship between the radar reflectivity factor Z and the scattering properties of target clouds is given by

$$Z = \frac{\lambda^4}{\pi^5|K|^2 V\sin^2\chi}\sigma, \quad (4)$$

where λ is the microwave wavelength and σ is the radar cross section (Gossard and Strauch, 1983), which is defined as

$$\sigma = 4\pi R^2\frac{P_{\rm s}}{P_{\rm o}}, \quad (5)$$

where $P_{\rm o}$ is the electric power of the incident microwave, which is given by $P_{\rm o} = |\mathbf{E}_{\rm inc}|^2/\zeta$. Substitution of Eqs. (2), (3), and (5) into Eq. (4) yields

$$Z = \frac{2^6}{V}\overline{\left|\int_{\mathbf{x}\in V}\int_0^\infty r_{\rm p}^3 n(\mathbf{x},r_{\rm p})\exp\left(-i\boldsymbol{\kappa}\cdot\mathbf{x}\right)dr_{\rm p}d\mathbf{x}\right|^2}, \quad (6)$$

where the wavenumber vector $\boldsymbol{\kappa}$ is defined as $\boldsymbol{\kappa} = \mathbf{k}_{\rm inc} - \mathbf{k}_{\rm sca}$. Note that radar remote sensing typically uses backward scattering; i.e., $\mathbf{k}_{\rm sca} = -\mathbf{k}_{\rm inc}$; thus, $\boldsymbol{\kappa} = 2\mathbf{k}_{\rm inc}$.

Similarly to Gossard and Strauch (1983), we assume $n(\mathbf{x},r_{\rm p})$ to be composed of the temporal-average and fluctuation parts; i.e., $n(\mathbf{x},r_{\rm p}) = \overline{n(\mathbf{x},r_{\rm p})} + \delta n(\mathbf{x},r_{\rm p})$. The temporal-average part, $\overline{n(\mathbf{x},r_{\rm p})}$, contributes to the separated reflection; therefore, the contribution of this part is negligibly small when $\overline{n(\mathbf{x},r_{\rm p})}$ has no fluctuation at a spatial scale of half the wavelength (Erkelens

Atmos. Chem. Phys. Discuss., https://doi.org/10.5194/acp-2018-480
Manuscript under review for journal Atmos. Chem. Phys.
Discussion started: 13 June 2018
© Author(s) 2018. CC BY 4.0 License.

et al., 2001). Thus, we neglect the contribution of $\overline{n(\mathbf{x},r_\mathrm{p})}$. Then, we obtain

$$Z = 2^6 \int_0^\infty \int_0^\infty \left\{ r_\mathrm{p}^3 r_\mathrm{p}'^3 \int_\mathbf{r} \langle \delta n(\mathbf{x},r_\mathrm{p}) \delta n(\mathbf{x}+\mathbf{r},r'_\mathrm{p}) \rangle \exp(-i\boldsymbol{\kappa}\cdot\mathbf{r})\, d\mathbf{r} \right\} dr_\mathrm{p} dr'_\mathrm{p}, \quad (7)$$

where the angular brackets represent a temporal and spatial average in the measurement volume.

In order to decompose the spatial correlation function $\langle \delta n(\mathbf{x},r_\mathrm{p}) \delta n(\mathbf{x}+\mathbf{r},r'_\mathrm{p}) \rangle$, we introduce the probability density function (PDF) of droplet radius r_p to the measurement volume, $q_\mathrm{r}(r_\mathrm{p})$, and the number density distribution function for monodisperse droplets with a radius of r_p, $n_\mathrm{p}(\mathbf{x}|r_\mathrm{p})$. The PDF is defined as $q_\mathrm{r}(r_\mathrm{p}) \equiv \frac{1}{N_\mathrm{p}} \int_{\mathbf{x}\in V} \overline{n(\mathbf{x},r_\mathrm{p})} d\mathbf{x}$, where N_p is the total number of droplets in the measurement volume; i.e., $N_\mathrm{p} \equiv \int_0^\infty \int_{\mathbf{x}\in V} \overline{n(\mathbf{x},r_\mathrm{p})} d\mathbf{x} dr_\mathrm{p}$. The PDF satisfies $\int_0^\infty q_\mathrm{r}(r_\mathrm{p}) dr_\mathrm{p} = 1$. The number density distribution function for monodisperse droplets is then defined as $n_\mathrm{p}(\mathbf{x}|r_\mathrm{p}) \equiv n(\mathbf{x},r_\mathrm{p})/q_\mathrm{r}(r_\mathrm{p})$ so that $n(\mathbf{x},r_\mathrm{p})$ is given by $n(\mathbf{x},r_\mathrm{p}) = n_\mathrm{p}(\mathbf{x}|r_\mathrm{p}) q_\mathrm{r}(r_\mathrm{p})$. The number density distribution function $n_\mathrm{p}(\mathbf{x}|r_\mathrm{p})$ satisfies $\int_{\mathbf{x}\in V} \overline{n_\mathrm{p}(\mathbf{x}|r_\mathrm{p})} d\mathbf{x} = N_\mathrm{p}$ for arbitrary r_p. Note that the spatial correlation function $\langle \delta n(\mathbf{x},r_\mathrm{p}) \delta n(\mathbf{x}+\mathbf{r},r'_\mathrm{p}) \rangle$ for $r'_\mathrm{p} = r_\mathrm{p}$ is discontinuous at $\mathbf{r} = \mathbf{0}$ because the droplet distribution is composed of spatially discrete points. The singularity is given by $\langle n(\mathbf{x},r_\mathrm{p}) \rangle \delta(\mathbf{r}) \delta(r'_\mathrm{p} - r_\mathrm{p})$, where $\delta(\mathbf{r})$ and $\delta(r'_\mathrm{p} - r_\mathrm{p})$ are the Dirac delta functions. Thus, the spatial correlation function is given by

$$\langle \delta n(\mathbf{x},r_\mathrm{p}) \delta n(\mathbf{x}+\mathbf{r},r'_\mathrm{p}) \rangle = \langle n_\mathrm{p} \rangle \delta(\mathbf{r}) q_\mathrm{r}(r_\mathrm{p}) \delta(r'_\mathrm{p} - r_\mathrm{p}) + \Psi(\mathbf{r}|r_\mathrm{p},r'_\mathrm{p}) q_\mathrm{r}(r_\mathrm{p}) q_\mathrm{r}(r'_\mathrm{p}), \quad (8)$$

where $\langle n_\mathrm{p} \rangle$ is the averaged number density ($\langle n_\mathrm{p} \rangle \equiv N_\mathrm{p}/V$) and $\Psi(\mathbf{r}|r_\mathrm{p},r'_\mathrm{p})$ is defined as the continuous part of $\langle \delta n_\mathrm{p}(\mathbf{x}|r_\mathrm{p}) \delta n_\mathrm{p}(\mathbf{x}+\mathbf{r}|r'_\mathrm{p}) \rangle$. Substitution of Eq. (8) into Eq. (7) and adoption of the isotropic clustering assumption (Gossard and Strauch, 1983) yield

$$Z = 2^6 \langle r_\mathrm{p}^6 \rangle \langle n_\mathrm{p} \rangle + 2^7 \pi^2 \kappa^{-2} E_\mathrm{r3np}(\kappa), \quad (9)$$

where κ is $\kappa = |\boldsymbol{\kappa}|$, $\langle r_\mathrm{p}^6 \rangle$ is given by $\langle r_\mathrm{p}^6 \rangle = \int_0^\infty r_\mathrm{p}^6 q_\mathrm{r}(r_\mathrm{p}) dr_\mathrm{p}$, and $E_\mathrm{r3np}(k)$ is the r_p^3-weighted power spectrum, defined as

$$E_\mathrm{r3np}(k) \equiv \int_0^\infty \int_0^\infty r_\mathrm{p}^3 r_\mathrm{p}'^3 q_\mathrm{r}(r_\mathrm{p}) q_\mathrm{r}(r'_\mathrm{p}) C_\mathrm{np}(k|r_\mathrm{p},r'_\mathrm{p}) dr_\mathrm{p} dr'_\mathrm{p}, \quad (10)$$

where $C_\mathrm{np}(k|r_\mathrm{p},r'_\mathrm{p})$ is the cross spectrum of number density fluctuations for $n_\mathrm{p}(\mathbf{x}|r_\mathrm{p})$ and $n_\mathrm{p}(\mathbf{x}|r'_\mathrm{p})$: The cross spectrum $C_\mathrm{np}(k|r_\mathrm{p},r'_\mathrm{p})$ is defined as $C_\mathrm{np}(k|r_\mathrm{p},r'_\mathrm{p}) \equiv \int_{|\mathbf{k}|=k} \widetilde{\Psi}(\mathbf{k}|r_\mathrm{p},r'_\mathrm{p}) d\sigma_k$; i.e., the integration of $\widetilde{\Psi}(\mathbf{k}|r_\mathrm{p},r'_\mathrm{p})$ over the spherical shell, σ_k, at $|\mathbf{k}| = k$, in which $\widetilde{\Psi}(\mathbf{k}|r_\mathrm{p},r'_\mathrm{p})$ is the cross spectral density function, defined as

$$\widetilde{\Psi}(\mathbf{k}|r_\mathrm{p},r'_\mathrm{p}) = \frac{1}{(2\pi)^3} \int_\mathbf{r} \Psi(\mathbf{r}|r_\mathrm{p},r'_\mathrm{p}) \exp(-i\mathbf{k}\cdot\mathbf{r})\, d\mathbf{r}. \quad (11)$$

The first and second terms on the right hand side of Eq. (9) are the incoherent and coherent scattering parts, respectively; particulate Bragg scattering is caused by the second term. Eqs. (9) and (10) imply that the particulate Bragg scattering part of Z for an arbitrary droplet size distribution can be calculated using the cross spectrum for bidisperse droplet size conditions. When droplets are distributed randomly and uniformly, the second term equals zero. Thus, the radar reflectivity factor when assuming a random and uniform droplet distribution is given by the first term; i.e., $Z_\mathrm{incoh} = 2^6 \langle r_\mathrm{p}^6 \rangle \langle n_\mathrm{p} \rangle$.

Atmos. Chem. Phys. Discuss., https://doi.org/10.5194/acp-2018-480
Manuscript under review for journal Atmos. Chem. Phys.
Discussion started: 13 June 2018
© Author(s) 2018. CC BY 4.0 License.

It should be noted that Eq. (9) satisfies the theoretical solution for particulate Bragg scattering of monodisperse droplets: For the case of monodisperse droplets with radii of r_{p1}, the PDF of droplet radius is given by $q_{\mathrm{r}}(r_{\mathrm{p}}) = \delta(r_{\mathrm{p}} - r_{\mathrm{p1}})$. Then, the radar reflectivity factor Z is given by

$$Z = 2^6 r_{\mathrm{p1}}^6 \langle n_{\mathrm{p}} \rangle + 2^7 \pi^2 \kappa^{-2} r_{\mathrm{p1}}^6 E_{\mathrm{np}}(\kappa | r_{\mathrm{p1}}), \tag{12}$$

where $E_{\mathrm{np}}(k|r_{\mathrm{p}})$ is the power spectrum of number density fluctuations, which satisfies $E_{\mathrm{np}}(k|r_{\mathrm{p}}) = C_{\mathrm{np}}(k|r_{\mathrm{p}}, r_{\mathrm{p}})$. Note that $E_{\mathrm{np}}(k|r_{\mathrm{p}})$ is defined as $E_{\mathrm{np}}(k|r_{\mathrm{p}}) \equiv \int_{|\mathbf{k}|=k} \widetilde{\Phi}(\mathbf{k}|r_{\mathrm{p}}) d\sigma_k$, where $\widetilde{\Phi}(\mathbf{k}|r_{\mathrm{p}})$ is the power spectral density function of $n_{\mathrm{p}}(\mathbf{x}|r_{\mathrm{p}})$, defined as

$$\widetilde{\Phi}(\mathbf{k}|r_{\mathrm{p}}) = \frac{1}{(2\pi)^3} \int_{\mathbf{r}} \Psi(\mathbf{r}|r_{\mathrm{p}}, r_{\mathrm{p}}) \exp(-i\mathbf{k}\cdot\mathbf{r})\, d\mathbf{r}. \tag{13}$$

3 Computational method

3.1 Direct numerical simulation

In order to obtain turbulent clustering data for calculating the cross spectrum, we have performed a three-dimensional DNS for particle-laden homogeneous isotropic turbulence. Three-dimensional incompressible turbulent air flows were calculated by solving the continuity and Navier-Stokes equations:

$$\frac{\partial u_i}{\partial x_i} = 0, \tag{14}$$

$$\frac{\partial u_i}{\partial t} + \frac{\partial u_i u_j}{\partial x_j} = -\frac{1}{\rho_{\mathrm{a}}}\frac{\partial p}{\partial x_i} + \nu \frac{\partial^2 u_i}{\partial x_j \partial x_j} + F_i, \tag{15}$$

where u_i is the flow velocity in the ith direction, p is the pressure, ρ_{a} is the air density, ν is the kinematic viscosity, and F_i is the external forcing term. The nonlinear term was discretized by the fourth-order central difference scheme (Morinishi et al., 1998). The time integration was calculated by the second-order Runge-Kutta scheme. The HSMAC method (Hirt and Cook, 1972) was used for velocity-pressure coupling. The external forcing was applied to maintain the intensity of large-scale eddies for wavenumbers $\mathbf{k}$ in the range $|\mathbf{k}L_0| < 2$ (Onishi et al., 2011), where L_0 is the representative length scale.

Droplet motions were simulated by Lagrangian point-particle tracking. Here, we assumed that the droplet density ρ_{p} is much larger than ρ_{a} and the drag term is given based on the Stokes law. The droplet motions were tracked by

$$\frac{dv_i}{dt} = -\frac{v_i - u_i}{\tau_{\mathrm{p}}} + g_i, \tag{16}$$

where v_i and g_i are the particle velocity and gravitational acceleration in the ith direction, respectively. τ_{p} is the droplet relaxation time, which is given by

$$\tau_{\mathrm{p}} = \frac{\rho_{\mathrm{p}}}{\rho_{\mathrm{a}}}\frac{2r_{\mathrm{p}}^2}{9\nu}. \tag{17}$$

The effects of turbulent modulation and droplet collision were neglected for simplicity because these effects were typically small in the time scale of τ_η in clouds. The gravitational acceleration was also neglected, i.e., $g_i = 0$. It should be noted

© Author(s) 2018. CC BY 4.0 License.

that Matsuda et al. (2014) and Matsuda et al. (2017) reported that the gravitational settling of cloud droplets can modulate enhancement of the radar reflectivity factor, and the influence can be significant under conditions of large gravitational settling velocity. However, according to the quantitative estimate of Matsuda et al. (2017), the influence would be smaller than 1 dB for cloud droplets ($r_{\rm p} < 40\mu$m) in cumulus clouds with strong turbulence. Thus, the influence of gravitational settling of these droplets is negligibly small.

The computational domain was set as a cube with edge lengths of $2\pi L_0$. Periodic boundary conditions were applied in all three directions. A uniform staggered grid was used for discretization. The number of grid points was set to 512^3. A Taylor microscale-based turbulent Reynolds number of the obtained flow was $\mathrm{Re}_\lambda = 204$, where Re_λ is defined as $\mathrm{Re}_\lambda \equiv l_\lambda u'/\nu$, where l_λ is the Taylor microscale and u' is the RMS value of the velocity fluctuation. Note that this value of Re_λ is sufficiently large to obtain turbulent clustering data for high Reynolds number turbulence in the wavenumber range relevant to radar observations (Matsuda et al., 2014) (see section 3.2). The kinematic viscosity, ν, was set to 1.5×10^{-5} m^2/s, and the ratio of the droplet density to the air density, $\rho_{\rm p}/\rho_{\rm a}$, was set to 840, assuming 1 atm and 298 K. The total number of droplets, $N_{\rm p}$, was set to 1.5×10^7.

For this study, we performed the DNS for monodisperse and polydisperse droplets. Table 1 shows the computational settings for turbulence and droplet size. For monodisperse droplets, the droplet motions in an identical turbulent flow field were calculated for six values of Stokes number, St. The clustering data for the monodisperse cases were used for calculating the cross spectrum of number density fluctuations for any combinations of these St. For polydisperse droplets, a typical droplet size distribution for maritime cumulus clouds (the size distribution data named "CUMA" in Hess et al. (1998)) was applied, and the droplets were tracked in turbulent flows using three different energy dissipation rates ϵ. ϵ values of the obtained turbulent flows were approximately 100, 400, and 1000 cm^2/s^3, which can be observed in cumulus and cumulonimbus clouds (Pinsky et al., 2008). The data for the polydisperse droplet cases were used to discuss the reliability of the proposed cross spectrum model. It should be noted that the droplet size distribution for the polydisperse cases were identical but the Stokes number histograms were different; the Stokes numbers corresponding to the modal radius (10.4 μm) for $\epsilon = 100$, 400, and 1000 cm^2/s^3 were 0.035, 0.069, and 0.10, respectively.

3.2 Computation of power spectrum and cross spectrum

The power spectral density function $\widetilde{\Phi}(\mathbf{k}|r_{\rm p})$ and the cross spectral density function $\widetilde{\Psi}(\mathbf{k}|r_{\rm p1}, r_{\rm p2})$ are calculated from the Lagrangian droplet distribution data as follows:

$$\widetilde{\Phi}(\mathbf{k}|r_{\rm p}) = L_0^{-3}\langle \widetilde{n_{\rm p}}(\mathbf{k}|r_{\rm p})\widetilde{n_{\rm p}}(-\mathbf{k}|r_{\rm p})\rangle, \quad (18)$$

$$\widetilde{\Psi}(\mathbf{k}|r_{\rm p1}, r_{\rm p2}) = L_0^{-3}\langle \widetilde{n_{\rm p}}(\mathbf{k}|r_{\rm p1})\widetilde{n_{\rm p}}(-\mathbf{k}|r_{\rm p2})\rangle, \quad (19)$$

where $\widetilde{n_{\rm p}}(\mathbf{k}|r_{\rm p})$ is the Fourier component of the droplet number density distribution, $n_{\rm p}(\mathbf{x}|r_{\rm p})$, and the angle brackets denote an ensemble average. The number density distribution for Lagrangian discrete droplets is given by

$$n_{\rm p}(\mathbf{x}|r_{\rm p}) = \sum_{j=1}^{N_{\rm p}} \delta(\mathbf{x} - \mathbf{x}_{{\rm p},j}), \quad (20)$$

Atmos. Chem. Phys. Discuss., https://doi.org/10.5194/acp-2018-480
Manuscript under review for journal Atmos. Chem. Phys.
Discussion started: 13 June 2018
© Author(s) 2018. CC BY 4.0 License.

Atmospheric Chemistry and Physics Discussions

Table 1. Computational settings of the DNS.

Case	L_0 (m)	ϵ (cm^2/s^3)	Droplet size
St005_eps400	0.0682	395	monodisperse (St $=0.05$)
St01_eps400			monodisperse (St $=0.10$)
St02_eps400			monodisperse (St $=0.20$)
St05_eps400			monodisperse (St $=0.50$)
St1_eps400			monodisperse (St $=1.0$)
St2_eps400			monodisperse (St $=2.0$)
CUMA_eps100	0.0961	100	polydisperse (CUMA)
CUMA_eps400	0.0682	395	polydisperse (CUMA)
CUMA_eps1000	0.0541	990	polydisperse (CUMA)

where $\mathbf{x}_{\mathrm{p},j}$ is the position vector of the jth droplet with radius r_p, and N_p is the total number of droplets with radius r_p. The Fourier components of Eq. (20) are then given by

$$\widetilde{n_\mathrm{p}}(\mathbf{k}|r_\mathrm{p}) = \frac{1}{(2\pi)^3}\sum_{j=1}^{N_\mathrm{p}} \exp(-i\mathbf{k}\cdot\mathbf{x}_{\mathrm{p},j}). \tag{21}$$

Substitution of Eq. (21) into Eq. (18) yields

$$\frac{\widetilde{\Phi}(\mathbf{k}|r_\mathrm{p})}{\langle n_\mathrm{p}\rangle^2 L_0^3} = \frac{1}{N_\mathrm{p}^2}\left\langle \sum_{j=1}^{N_\mathrm{p}} \exp\left(-i\mathbf{k}\cdot\mathbf{x}_{\mathrm{p},j}\right) \sum_{j'=1,j'\neq j}^{N_\mathrm{p}} \exp\left(i\mathbf{k}\cdot\mathbf{x}_{\mathrm{p},j'}\right)\right\rangle \tag{22}$$

$$= \frac{1}{N_\mathrm{p}^2}\left[\left\langle\left\{\sum_{j=1}^{N_\mathrm{p}}\cos(\mathbf{k}\cdot\mathbf{x}_{\mathrm{p},j})\right\}^2\right\rangle + \left\langle\left\{\sum_{j=1}^{N_\mathrm{p}}\sin(\mathbf{k}\cdot\mathbf{x}_{\mathrm{p},j})\right\}^2\right\rangle\right] - \frac{1}{N_\mathrm{p}}. \tag{23}$$

Similarly, substitution of Eq. (21) into Eq. (19) yields

$$\frac{\widetilde{\Psi}(\mathbf{k}|r_{\mathrm{p}1},r_{\mathrm{p}2})}{\langle n_{\mathrm{p}1}\rangle\langle n_{\mathrm{p}2}\rangle L_0^3} = \frac{1}{N_{\mathrm{p}1}N_{\mathrm{p}2}}\left\langle \sum_{j=1}^{N_{\mathrm{p}1}} \exp\left(-i\mathbf{k}\cdot\mathbf{x}_{\mathrm{p}1,j}\right) \sum_{j'=1}^{N_{\mathrm{p}2}} \exp\left(i\mathbf{k}\cdot\mathbf{x}_{\mathrm{p}2,j'}\right)\right\rangle \tag{24}$$

$$= \frac{1}{N_{\mathrm{p}1}N_{\mathrm{p}2}}\left\{\left\langle \sum_{j=1}^{N_{\mathrm{p}1}}\cos(\mathbf{k}\cdot\mathbf{x}_{\mathrm{p}1,j}) \sum_{j'=1}^{N_{\mathrm{p}2}}\cos(\mathbf{k}\cdot\mathbf{x}_{\mathrm{p}2,j'})\right\rangle + \left\langle \sum_{j=1}^{N_{\mathrm{p}1}}\sin(\mathbf{k}\cdot\mathbf{x}_{\mathrm{p}1,j}) \sum_{j'=1}^{N_{\mathrm{p}2}}\sin(\mathbf{k}\cdot\mathbf{x}_{\mathrm{p}2,j'})\right\rangle\right\}, \tag{25}$$

where $\langle n_{\mathrm{p}1}\rangle$ and $\langle n_{\mathrm{p}2}\rangle$ are the average number density of droplets with radii of $r_{\mathrm{p}1}$ and $r_{\mathrm{p}2}$ (i.e., $\langle n_{\mathrm{p}1}\rangle \equiv \langle n_\mathrm{p}(\mathbf{x}|r_{\mathrm{p}1})\rangle$ and $\langle n_{\mathrm{p}2}\rangle \equiv \langle n_\mathrm{p}(\mathbf{x}|r_{\mathrm{p}2})\rangle$), respectively, $N_{\mathrm{p}1}$ and $N_{\mathrm{p}2}$ are the numbers of droplets with radii of $r_{\mathrm{p}1}$ and $r_{\mathrm{p}2}$, respectively, $\mathbf{x}_{\mathrm{p}1,j}$ is the position of the jth droplet with a radius of $r_{\mathrm{p}1}$, and $\mathbf{x}_{\mathrm{p}2,j'}$ is the position of the j'th droplet with a radius of $r_{\mathrm{p}2}$. It should be noted that the imaginary part of $\widetilde{\Psi}(\mathbf{k}|r_{\mathrm{p}1},r_{\mathrm{p}2})$ is omitted in Eq. (25) because, statistically, it should be zero. We confirmed that the imaginary part of $C_{\mathrm{np}}(k|r_{\mathrm{p}1},r_{\mathrm{p}2})$ calculated from the DNS data is $O(10^{-4})$, which is caused by the statistical and truncation errors.

Atmos. Chem. Phys. Discuss., https://doi.org/10.5194/acp-2018-480
Manuscript under review for journal Atmos. Chem. Phys.
Discussion started: 13 June 2018
© Author(s) 2018. CC BY 4.0 License.

The spectral density functions, $\widetilde{\Phi}(\mathbf{k}|r_{\rm p})$ and $\widetilde{\Psi}(\mathbf{k}|r_{\rm p1},r_{\rm p2})$, were calculated for discrete wavenumbers $\mathbf{k}L_0 = (h_1, h_2, h_3)$, where h_1, h_2, and h_3 are arbitrary integers, that satisfy $k - \Delta k/2 \leq |\mathbf{k}| < k + \Delta k/2$, where Δk was set to $1/L_0$. $E_{\rm np}(k|r_{\rm p})$ and $C_{\rm np}(k|r_{\rm p1},r_{\rm p2})$ were then obtained by the following equations:

$$E_{\rm np}(k|r_{\rm p}) = \frac{1}{\Delta k} \sum_{k-\frac{1}{2}\Delta k \leq |\mathbf{k}| < k+\frac{1}{2}\Delta k} \widetilde{\Phi}(\mathbf{k}|r_{\rm p}), \tag{26}$$

$$C_{\rm np}(k|r_{\rm p1},r_{\rm p2}) = \frac{1}{\Delta k} \sum_{k-\frac{1}{2}\Delta k \leq |\mathbf{k}| < k+\frac{1}{2}\Delta k} \widetilde{\Psi}(\mathbf{k}|r_{\rm p1},r_{\rm p2}). \tag{27}$$

The spectra, $E_{\rm np}(k|r_{\rm p})$ and $C_{\rm np}(k|r_{\rm p1},r_{\rm p2})$, were calculated for 19 representative wavenumbers in the same way as Matsuda et al. (2014). The ensemble average in Eq. (23) was obtained by averaging 10 temporal slices of the droplet distributions, which were sampled for intervals of $T_0 = L_0/U_0$. The ensemble average in Eq. (25) was also obtained for 10 pairs of temporal slices. Each pair was composed of temporal slices at the same time step for different St cases.

Matsuda et al. (2014) normalized the power spectrum $E_{\rm np}(k|r_{\rm p})$ by using $\langle n_{\rm p}\rangle$ and the Kolmogorov scale, l_η, defined as $l_\eta \equiv \nu^{3/4}\epsilon^{-1/4}$, and confirmed that, for $\mathrm{Re}_\lambda \geq 204$, the Re_λ dependence of the normalized power spectrum is negligible at the wavenumber range relevant to radar observations ($0.05 < kl_\eta < 4.0$). Thus, this study used the same normalization for $E_{\rm np}(k|r_{\rm p})$ and $C_{\rm np}(k|r_{\rm p1},r_{\rm p2})$ as follows:

$$E^*_{\rm np}(\xi|\mathrm{St}) = E^*_{\rm np}(kl_\eta|\mathrm{St}) \equiv \frac{E_{\rm np}(k|r_{\rm p})}{\langle n_{\rm p}\rangle^2 l_\eta}, \tag{28}$$

$$C^*_{\rm np}(\xi|\mathrm{St}_1,\mathrm{St}_2) = C^*_{\rm np}(kl_\eta|\mathrm{St}_1,\mathrm{St}_2) \equiv \frac{C_{\rm np}(k|r_{\rm p1},r_{\rm p2})}{\langle n_{\rm p1}\rangle\langle n_{\rm p2}\rangle l_\eta}, \tag{29}$$

where ξ is the normalized wavenumber defined as $\xi \equiv kl_\eta$ and St, St_1, and St_2 are the Stokes numbers of water droplets with radii of $r_{\rm p}$, $r_{\rm p1}$, and $r_{\rm p2}$, respectively.

4 Results and discussion

4.1 Spatial droplet distribution and cross spectrum

Figure 1 shows the spatial distribution of droplets for $\mathrm{St} = 0.2$, 0.5, and 1.0. Droplets located in the range of $0 < z < 4l_\eta$ are indicated. The droplet position data were sampled at the same time step; i.e., the background turbulent flow field is identical. Figure 1(a) is the overall view of the region with a size of $2\pi L_0 \times 2\pi L_0$, while Figure 1(b) is the magnified view for the region with a size of $0.5\pi L_0 \times 0.5\pi L_0$. The clusters and void areas are clearly observed for all St cases. Their location for $\mathrm{St} = 0.5$ is almost the same as that for the other St. This is because the locations of clusters and void areas for small St are strongly dependent on the instantaneous turbulent flow field. However, the small-scale structure of clusters is not exactly the same; i.e., the droplets become more concentrated in clusters as St increases. Figure 2 shows the power spectra $E^*_{\rm np}(\xi|\mathrm{St})$ and the cross spectra $C^*_{\rm np}(\xi|\mathrm{St}_1,\mathrm{St}_2)$ obtained from the DNS data. Note that the high wavenumber portion is omitted when the value of the cross spectrum is smaller than the computational error level (10^{-4}). The power spectra $E^*_{\rm np}(\xi|\mathrm{St})$ show power law type slopes at wavenumbers smaller and larger than the peak location. The peak height and slope of the spectra are strongly dependent

© Author(s) 2018. CC BY 4.0 License.

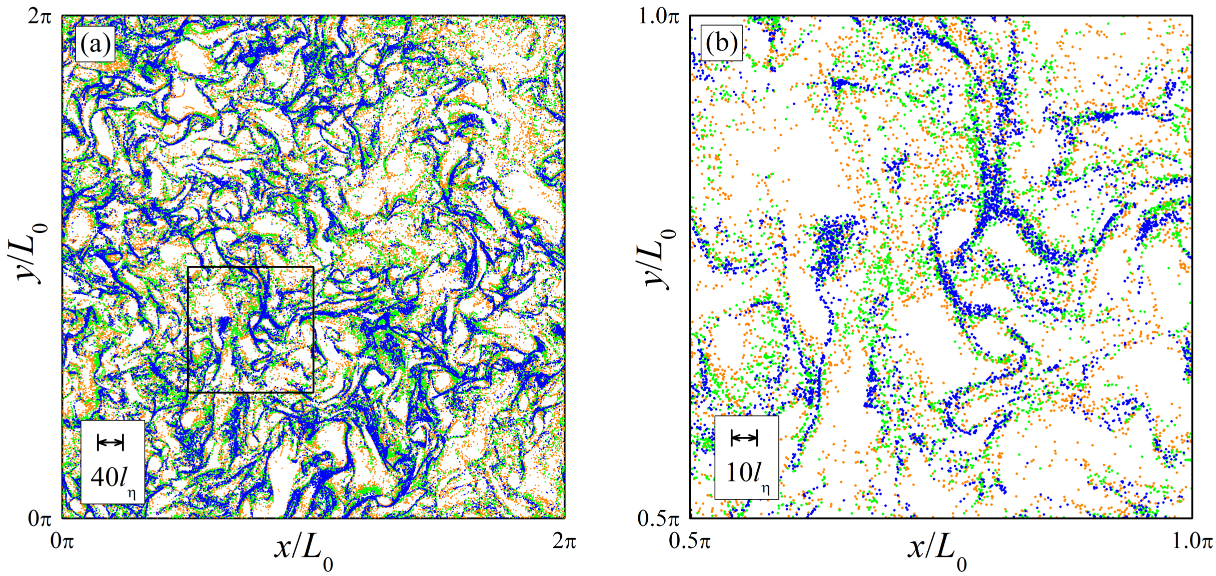

Figure 1. Spatial distribution of droplets for (orange) St = 0.2, (green) 0.5, and (blue) 1.0 in the regions of (a) $2\pi L_0 \times 2\pi L_0$ and (b) $0.5\pi L_0 \times 0.5\pi L_0$. Droplets located in the range of $0 < z < 4l_\eta$ are shown. The square frame in (a) corresponds to the region of (b).

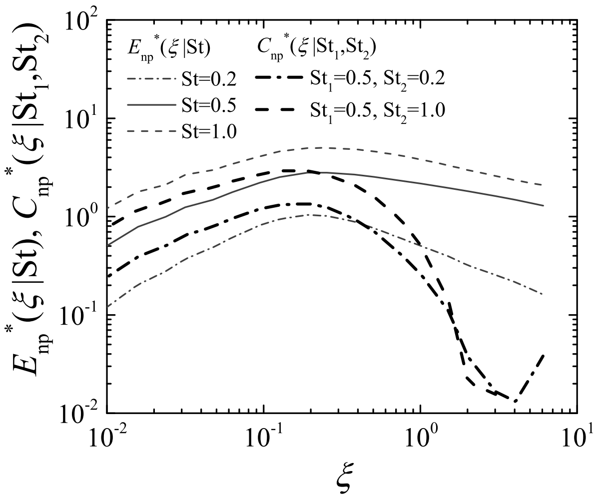

Figure 2. Normalized cross spectra $C^*_{\mathrm{np}}(\xi|\mathrm{St}_1,\mathrm{St}_2)$ of droplet number density fluctuations compared to normalized power spectra $E^*_{\mathrm{np}}(\xi|\mathrm{St})$.

Atmos. Chem. Phys. Discuss., https://doi.org/10.5194/acp-2018-480
Manuscript under review for journal Atmos. Chem. Phys.
Discussion started: 13 June 2018
© Author(s) 2018. CC BY 4.0 License.

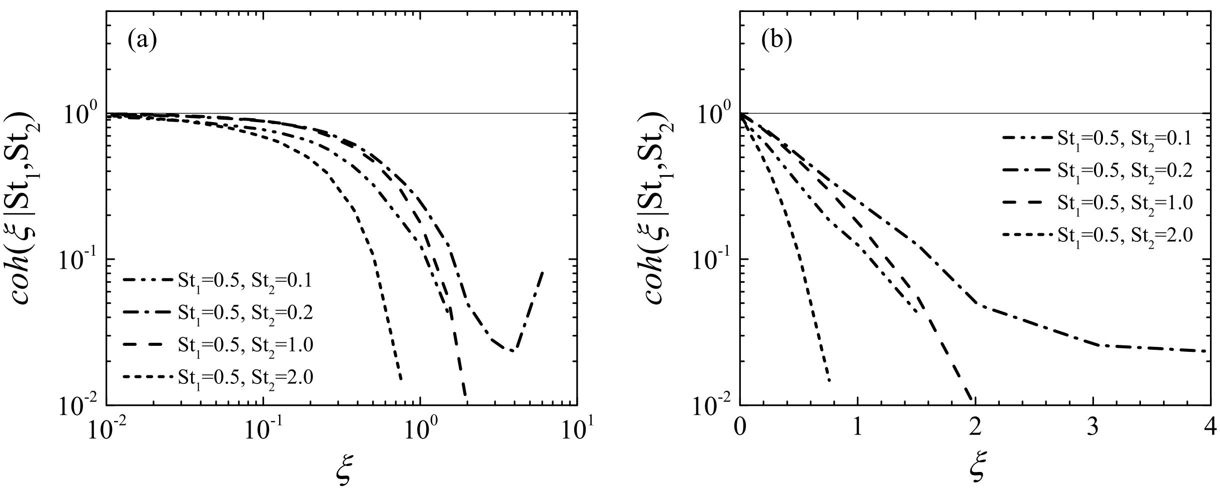

Figure 3. Coherence of cross spectra for combinations of $\mathrm{St}_1 = 0.5$ and other Stokes numbers. The same coherence is plotted in (a) a double logarithmic chart and (b) a vertically logarithmic chart.

on the Stokes number; this Stokes number dependence was discussed by Matsuda et al. (2014). In the small wavenumber region, the cross spectra C^*_{np} also show power law type slopes. In this region, the curve of C^*_{np} for $\mathrm{St}_1 = 0.5$ and $\mathrm{St}_2 = 0.2$ is located between the power spectra E^*_{np} for $\mathrm{St} = 0.5$ and $\mathrm{St} = 0.2$. Similarly, the curve of C^*_{np} for $\mathrm{St}_1 = 0.5$ and $\mathrm{St}_2 = 1.0$ is located between the power spectra E^*_{np} for $\mathrm{St} = 0.5$ and $\mathrm{St} = 1.0$. On the other hand, in the large wavenumber region, both cross spectra C^*_{np} become smaller than the power spectra E^*_{np} without showing power law type slopes. These trends imply that the cross spectrum is influenced by not only the Stokes number dependence of the clustering intensity, but also the spatial correlation of clusters between different values of St. In order to focus on the influence of the spatial correlation of clusters, we have evaluated the coherence $coh(\xi|\mathrm{St}_1,\mathrm{St}_2)$, which is defined as

$$coh(\xi|\mathrm{St}_1,\mathrm{St}_2) = \frac{|C^*_{\mathrm{np}}(\xi|\mathrm{St}_1,\mathrm{St}_2)|}{\sqrt{E^*_{\mathrm{np}}(\xi|\mathrm{St}_1)E^*_{\mathrm{np}}(\xi|\mathrm{St}_2)}}. \tag{30}$$

Figure 3 shows the coherence between $\mathrm{St}_1 = 0.5$ and other Stokes numbers. The coherence $coh(\xi|\mathrm{St}_1,\mathrm{St}_2)$ is close to unity in the small wavenumber region and decreases to zero as the wavenumber increases. These trends correspond to the spatial correlation between cluster locations for different St cases in Figure 1. Figure 3(b) shows that the coherence decreases with an almost constant slope in the vertically logarithmic and horizontally linear chart. The slope of the coherence is dependent on the combination of St_1 and St_2; the slope becomes steeper as the difference of St increases. These results indicate that the decreasing trend of coherence can be approximated by an exponential function; i.e.,

$$coh(\xi|\mathrm{St}_1,\mathrm{St}_2) \approx \exp(-\xi/\xi_c), \tag{31}$$

Atmos. Chem. Phys. Discuss., https://doi.org/10.5194/acp-2018-480
Manuscript under review for journal Atmos. Chem. Phys.
Discussion started: 13 June 2018
© Author(s) 2018. CC BY 4.0 License.

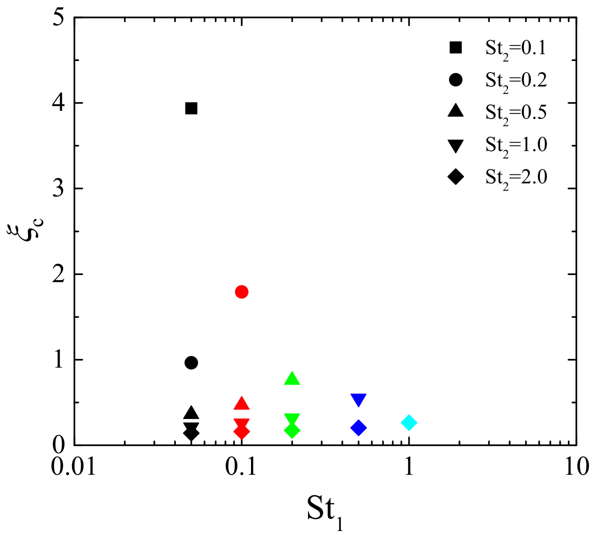

Figure 4. Critical wavenumber ξ_c for a combination of Stokes numbers, St_1 and St_2. The symbol color and type indicate the combination of Stokes numbers. The black, red, green, blue, and light blue symbols are $\mathrm{St}_1 = 0.05$, 0.1, 0.2, 0.5, and 1.0, respectively. The square, circle, triangle, inverse triangle, and diamond symbols are $\mathrm{St}_2 = 0.1$, 0.2, 0.5, 1.0, and 2.0, respectively.

where ξ_c is the critical wavenumber normalized by the Kolmogorov scale, given by a function of St_1 and St_2. In this study, the critical wavenumber was obtained by finding the best-fitting exponential curve to the coherence for each combination of Stokes numbers. Figure 4 shows the critical wavenumbers ξ_c for all combinations of St_1 and St_2, where $\mathrm{St}_2 > \mathrm{St}_1$. ξ_c for the same St_1 increases as St_2 decreases; whereas ξ_c for the same St_2 increases as St_1 increases. This indicates that ξ_c increases as St_1 and St_2 becomes closer each other. It should be noted that several studies discuss the spatial correlation of bidisperse clustering particles. For example, Zhou et al. (2001) developed the radial distribution function (RDF) model at the separation length of the Kolmogorov scale. They reported that the correlation coefficient of the bidisperse RDF obtained by their DNS is explained well by the ratio of two Stokes numbers. Chun et al. (2005) also discussed the bidisperse RDF of clustering particles. The result of their perturbation expansion analysis indicated that the bidisperse RDF becomes constant at separation lengths sufficiently smaller than the "cross-over length," l_c, which is proportional to the Stokes number difference. As the cross spectrum of number density fluctuations is a Fourier transform of the bidisperse RDF, the Stokes number ratio, $\mathrm{St}_2/\mathrm{St}_1$, and the Stokes number difference, $\mathrm{St}_2 - \mathrm{St}_1$, are candidates for the dominant parameter for ξ_c. Figure 5 shows ξ_c plots against $\mathrm{St}_2/\mathrm{St}_1$ and $\mathrm{St}_2 - \mathrm{St}_1$. These figures clearly indicate that the Stokes number dependence of ξ_c is explained by $\mathrm{St}_2 - \mathrm{St}_1$ better than $\mathrm{St}_2/\mathrm{St}_1$. This would be because both the critical wavenumber ξ_c and cross-over length l_c represent the critical scale of the spatial correlation between the clusters for different Stokes numbers; i.e., the cluster locations are less correlated at a scale smaller than the critical scale. Based on this insight, we estimate that the critical wavenumber ξ_c is inversely proportional to the cross-over length l_c. Figure 6 shows ξ_c against the inverse of the Stokes number difference, which is generally expressed

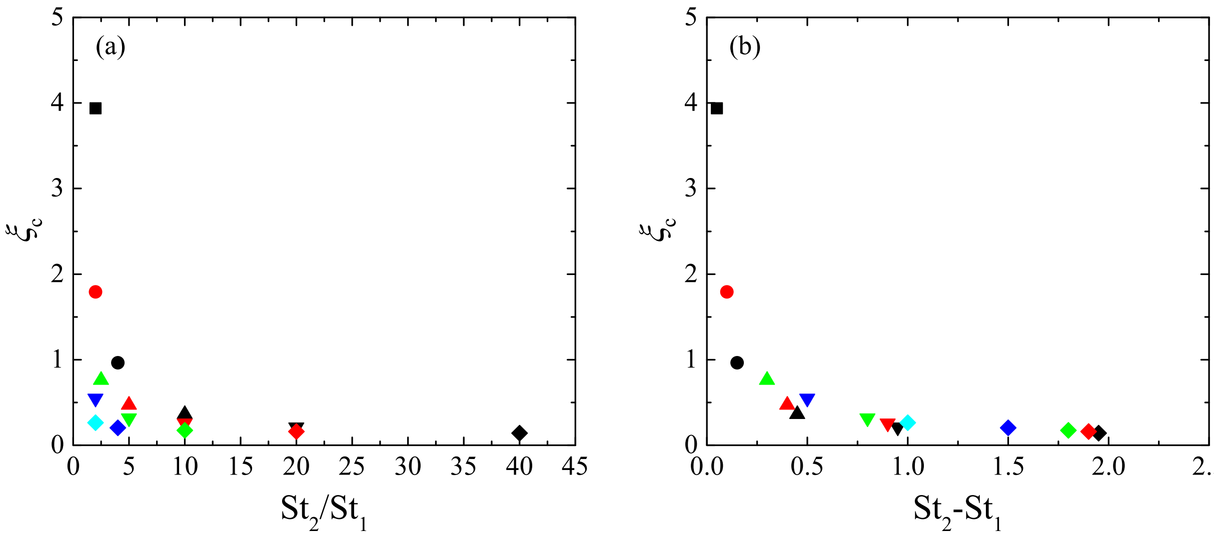

Figure 5. (a) Critical wavenumber ξ_c against the Stokes number ratio $\mathrm{St}_2/\mathrm{St}_1$, and (b) against the Stokes number difference $\mathrm{St}_2 - \mathrm{St}_1$. Notations are as in Fig. 4.

as $1/|\mathrm{St}_1 - \mathrm{St}_2|$. This figure confirms that ξ_c is approximately proportional to $1/|\mathrm{St}_1 - \mathrm{St}_2|$; the least square fitting gives

$$\xi_c(\mathrm{St}_1, \mathrm{St}_2) \approx \frac{0.191}{|\mathrm{St}_1 - \mathrm{St}_2|}. \tag{32}$$

This implies that ξ_c is closely related to the inverse of l_c/l_η because the cross-over length of Chun et al. (2005) is approximately $l_c/l_\eta \approx 5.0|\mathrm{St}_1 - \mathrm{St}_2|$ based on their DNS data. It should be noted that the analytical results of Chun et al. (2005) are valid for $\mathrm{St} \ll 1$. Thus, the deviation of ξ_c from the linear curve is due to the higher-order response of particle motions to the turbulent flow. However, Fig. 6 confirms that the Stokes number difference is the dominant parameter for ξ_c; at least for $\mathrm{St} \leq 2.0$.

4.2 Modeling the influence of polydisperse clustering droplets on radar reflectivity factor

According to the above discussion, we can estimate the increase in the radar reflectivity factor due to turbulent clustering of polydispere droplets in Eq. (9), provided that $q_r(r_p)$ and $\langle n_p \rangle$ are given. That is, the normalized cross spectrum $C^*_{np}(\xi|\mathrm{St}_1, \mathrm{St}_2)$ can be estimated by

$$C^*_{np}(\xi|\mathrm{St}_1, \mathrm{St}_2) = coh(\xi|\mathrm{St}_1, \mathrm{St}_2)\sqrt{E^*_{np}(\xi|\mathrm{St}_1) E^*_{np}(\xi|\mathrm{St}_2)}. \tag{33}$$

Here, we assume that the cross spectrum is a positive real number. The coherence is estimated using Eqs. (31) and (32). The parameterization for $E^*_{np}(\xi|\mathrm{St})$ was proposed by Matsuda et al. (2014). The model equations are summarized in Appendix A.

In order to evaluate the reliability of the proposed cross spectrum model, the r_p^3-weighted power spectrum $E_{r3np}(k)$ for the droplet size distribution of CUMA has been estimated using the proposed cross spectrum model and compared with the spectrum obtained from the DNS data for the cases of CUMA_eps100, CUMA_eps400, and CUMA_eps1000. Figure 7 shows

© Author(s) 2018. CC BY 4.0 License.

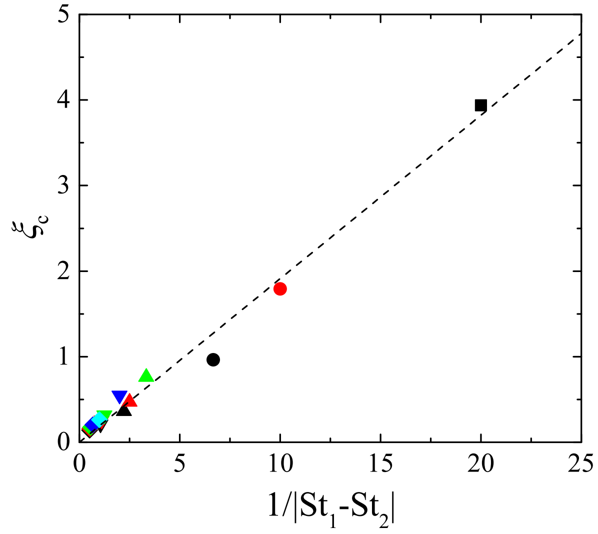

Figure 6. Critical wavenumber ξ_c against the inverse of Stokes number difference. The dashed line is the best-fitting curve to the ξ_c data. Other notations are as in Fig. 4.

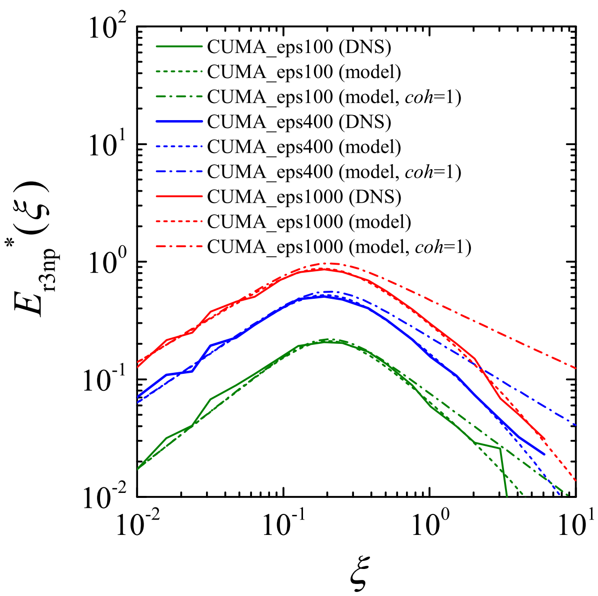

Figure 7. Comparisons of r_p^3-weighted power spectrum $E^*_{r3np}(\xi)$ obtained from DNS data and that estimated by the proposed cross spectrum model.

Atmos. Chem. Phys. Discuss., https://doi.org/10.5194/acp-2018-480
Manuscript under review for journal Atmos. Chem. Phys.
Discussion started: 13 June 2018
© Author(s) 2018. CC BY 4.0 License.

Atmospheric Chemistry and Physics
Discussions

the r_p^3-weighted power spectrum, which is normalized as

$$E^*_{\mathrm{r3np}}(\xi) = \frac{E_{\mathrm{r3np}}(k)}{\langle r_\mathrm{p}^3\rangle^2 \langle n_\mathrm{p}\rangle^2 l_\eta}, \tag{34}$$

where $\langle r_\mathrm{p}^3\rangle$ is given by $\langle r_\mathrm{p}^3\rangle = \int_0^\infty r_\mathrm{p}^3 q_\mathrm{r}(r_\mathrm{p}) dr_\mathrm{p}$. The dashed lines show $E^*_{\mathrm{r3np}}(\xi)$ predicted using the proposed parameterization including Eq. (31), while the dashed-dotted lines show those predicted by assuming perfect coherence, i.e., $coh(\xi|\mathrm{St}_1, \mathrm{St}_2) = 1$. The parameterization with $coh(\xi|\mathrm{St}_1, \mathrm{St}_2) = 1$ overestimates $E^*_{\mathrm{r3np}}(\xi)$ at large wavenumbers and the difference becomes larger as ϵ becomes larger. This indicates that the influence of the weak spatial correlation of cluster locations between different Stokes numbers is not negligible for predicting the spectrum $E^*_{\mathrm{r3np}}(\xi)$ for large wavenumbers, and the assumption of $coh(\xi|\mathrm{St}_1, \mathrm{St}_2) = 1$ can be applied only for predicting $E^*_{\mathrm{r3np}}(\xi)$ for small wavenumbers ($\xi < O(10^{-1})$). On the other hand, $E^*_{\mathrm{r3np}}(\xi)$ values predicted by the parameterization using Eq. (31) show good agreement with those obtained by the DNS data for overall wavenumbers. The error level of the parameterization using Eq. (31) is evaluated by the RMS error e_RMS in units of decibels. e_RMS is defined as

$$e_\mathrm{RMS} = \frac{1}{\xi'_\mathrm{max} - \xi'_\mathrm{min}} \int_{\xi'_\mathrm{min}}^{\xi'_\mathrm{max}} \left\{ {E^*_{\mathrm{r3np,model}}}^{\mathrm{dB}}(\xi) - {E^*_{\mathrm{r3np,DNS}}}^{\mathrm{dB}}(\xi) \right\}^2 d\xi', \tag{35}$$

where ξ' is defined as $\xi' = \ln \xi$ and superscript dB denotes a value in units of decibels. e_RMS was calculated for the wavenumber range relevant to radar observations; i.e., $0.05 \le \xi \le 4.0$. e_RMS for the cases of CUMA_eps100, CUMA_eps400, and CUMA_eps1000 are 1.41, 0.152, and 0.251 dB, respectively. Because the error level of 1 dB is unavoidable for radar observations (Bringi et al., 1990; Carey et al., 2000), e_RMS values for CUMA_eps400 and CUMA_eps1000 are negligibly small. e_RMS for CUMA_eps100 is slightly larger than the threshold, but this is caused by the error of calculating the reference spectrum based on the DNS data at $\xi > 2$. We confirm that, for CUMA_eps100, e_RMS evaluated at the range of $0.05 \le \xi \le 2.0$ is smaller than 1 dB. Thus, the proposed parameterization can predict the influence of turbulent clustering for polydisperse droplets to a sufficient accuracy.

4.3 Application to cloud simulation data

We have applied the proposed model to the high-resolution cloud-simulation data of Onishi and Takahashi (2012) to investigate the influence of turbulent clustering on radar observations. They used the Multi-Scale Simulator for the Geoenvironment (MSSG), which is a multi-scale atmosphere-ocean coupled model developed by the Japan Agency for Marine-Earth Science and Technology. The atmospheric component of MSSG (MSSG-A) solves non-hydrostatic equations and predicts three wind components, air density, and pressure, as well as water substance. Finite difference schemes are used for calculating spatial derivatives. Turbulent diffusion is calculated using the static Smagorinsky model. Onishi and Takahashi (2012) used a spectral-bin scheme for liquid water to explicitly account for the droplet size distributions. The spectral bin scheme predicts the mass distribution function $g(y)$, which is given by

$$g(y)dy = n_\mathrm{p} m(r_\mathrm{p}) q_\mathrm{r}(r_\mathrm{p}) dr_\mathrm{p} \tag{36}$$

© Author(s) 2018. CC BY 4.0 License.

where $y = \ln r_\mathrm{p}$, and $m(r_\mathrm{p})$ is the mass of droplets with a radius of r_p. The mass coordinate m and logarithmic coordinate y are discretized as

$$m_k = 2^{1/s} m_{k-1} \tag{37}$$

$$y_k = y_{k-1} + dy \tag{38}$$

where $dy = \ln 2/(3s)$, and s is a constant; $s = 1$ were used. The number of bins was 33. The representative radius of the first bin, r_p1, was 3 μm; thus, the representative radius of the 33rd bin (the largest droplet class) was $r_\mathrm{p33} = 4.9$ mm. The prognostic variable for liquid water is the water mass content, M_k, which is defined as $M_k = \int_{y_{k-1/2}}^{y_{k+1/2}} g(y)dy$; i.e., 33 transport equations for M_k were solved in this simulation. The model settings and computational conditions were based on the protocol of the RICO model intercomparison project (van Zanten et al., http://www.knmi.nl/samenw/rico/). The protocol is based on the rain in cumulus over the ocean (RICO) field campaign. The domain size is $12.8 \times 12.8 \times 4.0$ km. The resolution setting of the original RICO protocol is 128×128 points in horizontal directions and 100 points in the vertical direction; i.e., $\Delta_\mathrm{x} = \Delta_\mathrm{y} = 100$ m and $\Delta_\mathrm{z} = 40$ m. Onishi and Takahashi (2012) performed the cloud simulation for 24 h using the original resolution setting, then continued it for an additional hour using a higher resolution setting, generating 512×512 points in horizontal directions and 200 points in the vertical direction, giving grid spacing of $\Delta_\mathrm{x} = \Delta_\mathrm{y} = 25$ m and $\Delta_\mathrm{z} = 20$ m. This study used the temporal slice of cloud simulation data at higher resolution.

In order to determine the Stokes number for each droplet size, the energy dissipation rate ϵ of the cloud simulation data was calculated as follows:

$$\epsilon = \epsilon_\mathrm{GS} + \epsilon_\mathrm{SGS}, \tag{39}$$

where ϵ_GS and ϵ_SGS are the components of ϵ in the grid scale (GS) and the sub-grid scale (SGS), respectively. ϵ_GS was calculated by

$$\epsilon_\mathrm{GS} = \nu \frac{\partial \widehat{u_i}}{\partial x_j} \frac{\partial \widehat{u_j}}{\partial x_i}, \tag{40}$$

where $\widetilde{u_i}$ is the air velocity in GS. ϵ_SGS was calculated based on the Smagorinsky model; i.e.,

$$\epsilon_\mathrm{SGS} = (C_\mathrm{s}\Delta_\mathrm{s})^2 \left(2\widehat{s_{ij}}\widehat{s_{ij}}\right)^{3/2}, \tag{41}$$

where C_s is the Smagorinsky constant ($C_\mathrm{s} = 0.173$ in this study), Δ_s the representative grid spacing given by $\Delta_\mathrm{s} = (\Delta_\mathrm{x}\Delta_\mathrm{y}\Delta_\mathrm{z})^{1/3}$, and $\widehat{s_{ij}}$ the strain rate tensor, which is given by $\widehat{s_{ij}} = \frac{1}{2}(\frac{\partial \widehat{u_i}}{\partial x_j} + \frac{\partial \widehat{u_j}}{\partial x_i})$. Figure 8(a) shows the three-dimensional visualization of liquid water. The optical thickness of each grid cell is visualized by volume rendering to mimic human-eye observations of clouds. Figure 8(b) shows the isosurfaces of the energy dissipation rate ϵ and the vertical velocity u_3. The locations of upward flows correspond to the locations of clouds and large ϵ regions are observed around the upward flows. This indicates that strong turbulence is generated by entrainment motions due to updrafts.

This study focused on a vertical cross section that slices the cumulus cloud with the largest upward velocity. Figure 9 shows the liquid water content (LWC), the energy dissipation rate ϵ, the radar reflectivity factor Z^dB, and the increase of Z^dB due

Atmos. Chem. Phys. Discuss., https://doi.org/10.5194/acp-2018-480
Manuscript under review for journal Atmos. Chem. Phys.
Discussion started: 13 June 2018
© Author(s) 2018. CC BY 4.0 License.

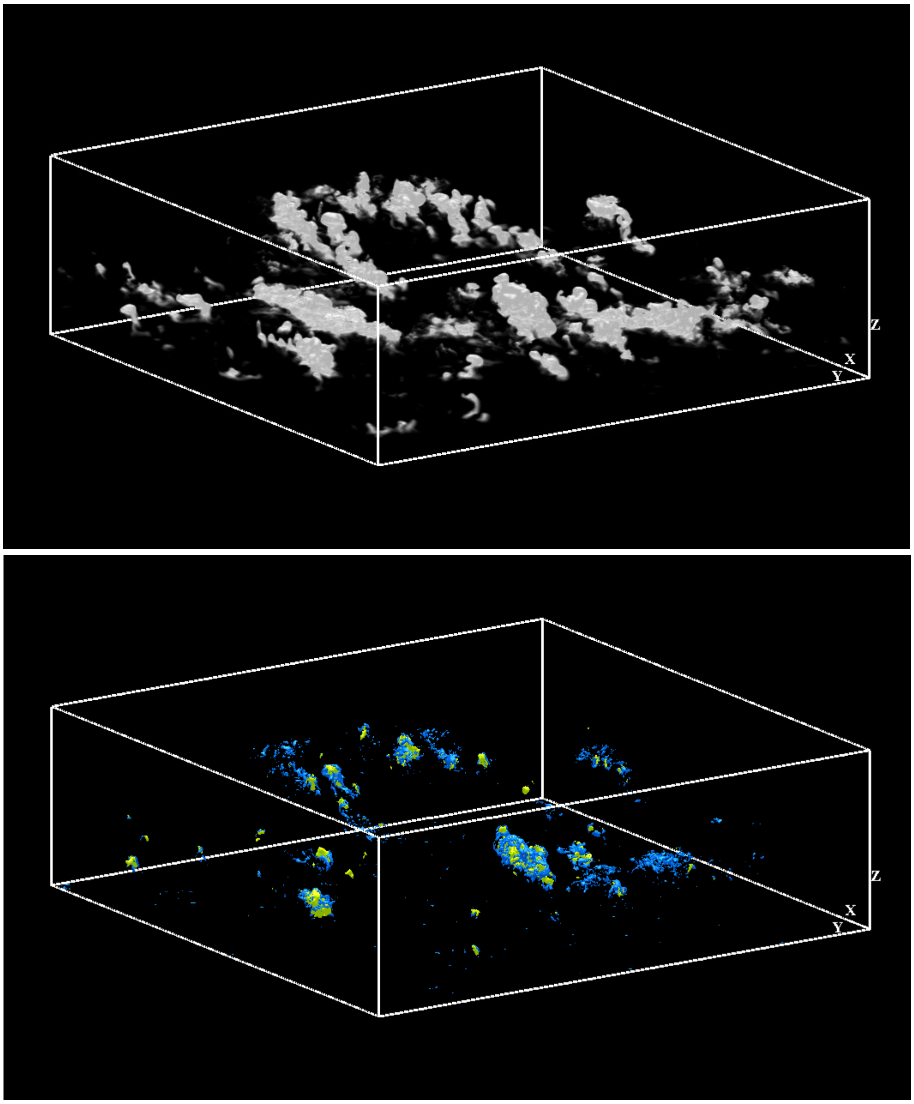

(a)
(b)

Figure 8. Three-dimensional visualization of cloud simulation data: (a) volume rendering of optical depth and (b) isosurfaces of (blue) the energy dissipation rate $\epsilon = 100$ cm^2/s^3 and (yellow) the vertical velocity $u_3 = 3$ m/s.

to turbulent clustering in the cross section. The microwave frequency was set to $f_\mathrm{m} = 2.8$ GHz, which is the representative frequency of S-band radars. The radar reflectivity factor is shown in units of decibels, which is defined as $Z^\mathrm{dB}\ (\mathrm{dBZ}) = 10\log_{10} Z(\mathrm{mm}^6/\mathrm{m}^3)$. Large values of Z^dB are observed inside and below the clouds. The strong echo below the clouds reflects drizzling regions, where the LWC is smaller than inside the clouds but the droplet size is larger than cloud droplets. The increase due to turbulent clustering, $Z^\mathrm{dB} - Z^\mathrm{dB}_\mathrm{incoh}$, is significant at the near-top of the clouds with large ϵ (i.e., strong turbulence). It should be noted that, as Eq. (9) can be rewritten as $Z = Z_\mathrm{incoh} + Z_\mathrm{Bragg}$, where Z_Bragg is the particulate Bragg

© Author(s) 2018. CC BY 4.0 License.

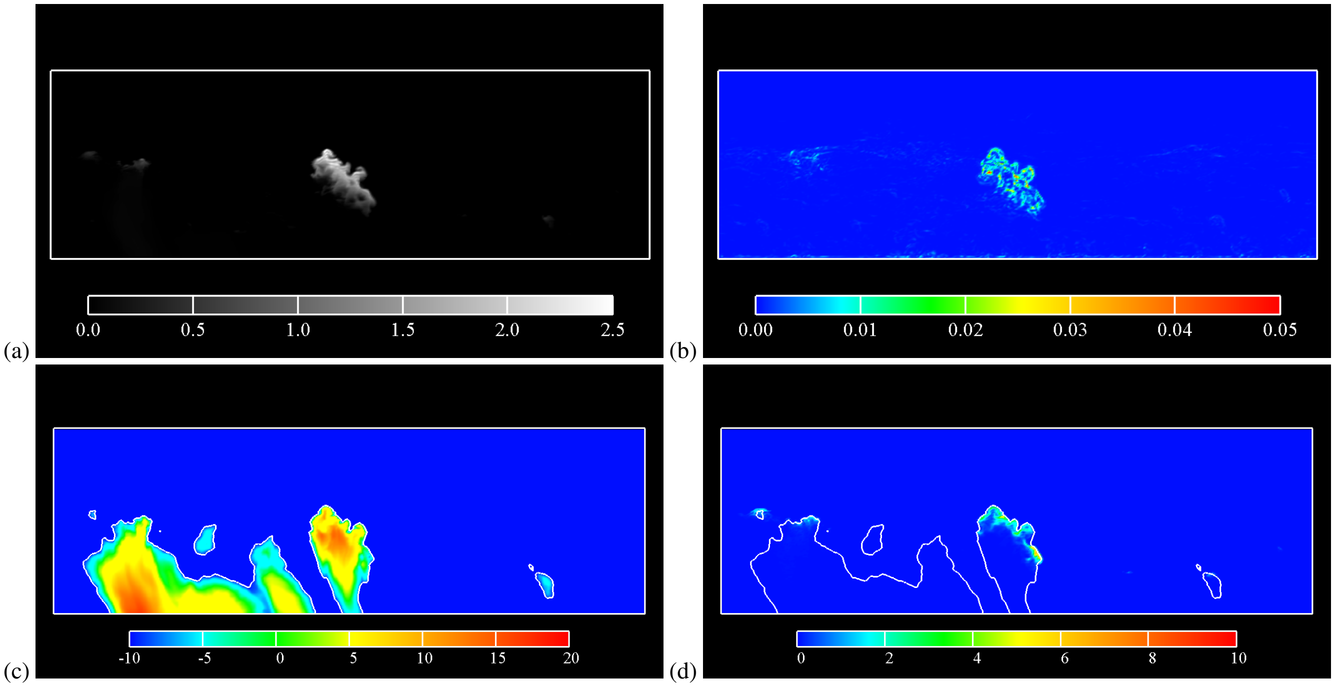

Figure 9. Liquid water content (LWC), energy dissipation rate ϵ, and radar reflectivity factors for S-band microwaves in the vertical cross section; (a) LWC (g/m^3), (b) ϵ (m^2/s^3), (c) $Z^{\rm dB}$ (dBZ), and (d) $Z^{\rm dB} - Z^{\rm dB}_{\rm incoh}$ (dB). The solid lines in (c) and (d) indicate the isoline of $Z^{\rm dB} = -10$ dBZ.

scattering part of Z, the increment satisfies $Z^{\rm dB} - Z^{\rm dB}_{\rm incoh} = (1 + Z_{\rm Bragg}/Z_{\rm incoh})^{\rm dB}$. Thus, the large values of $Z^{\rm dB} - Z^{\rm dB}_{\rm incoh}$ indicate that $Z_{\rm Bragg}$ is much larger than $Z_{\rm incoh}$. In contrast, the increment, $Z^{\rm dB} - Z^{\rm dB}_{\rm incoh}$, is not significant in drizzling regions. This is because $Z_{\rm incoh}$ is proportional to $\langle r_{\rm p}^6 \rangle$, whereas $Z_{\rm Bragg}$ is proportional to $\langle r_{\rm p}^3 \rangle^2$ (if $E^*_{\rm r3np}(\xi)$ constant). In other words, for cloud portions that contain large droplets such as drizzle, $Z_{\rm incoh}$ is much larger than $Z_{\rm Bragg}$. Thus, enhancement of the radar reflectivity factor due to turbulent droplet clustering is negligibly small for cloud portions with drizzle particles.

5 Conclusions

This study has investigated the influence of microscale turbulent clustering of polydisperse cloud droplets on the radar reflectivity factor. Firstly, the theoretical solution for particulate Bragg scattering for polydisperse droplets has been obtained considering the droplet size distribution in the measurement volume and the droplet size dependence of turbulent clustering. The obtained formula shows that the particulate Bragg scattering part of the radar reflectivity factor is given by a double integral function including the cross spectrum of number density fluctuations for bidisperse droplets. Secondly, the wavenumber and Stokes number dependence of the cross spectrum has been investigated using the turbulent droplet clustering data obtained from a direct numerical simulation (DNS) of particle-laden homogeneous isotropic turbulence. The result shows that the cross spectrum for a combination of Stokes numbers, St_1 and St_2, has values between the power spectra for St_1 and St_2 at small wavenumbers, whereas the spectrum decreases more rapidly than the power spectra as the wavenumber increases. This decreasing trend is related to the scale dependence of the spatial correlation of cluster locations between two different Stokes numbers. The coherence of the cross spectrum is close to unity for small wavenumbers and decreases almost exponentially with increasing wavenumber. This is qualitatively consistent with the visualization results, in which the clustering locations for different Stokes numbers are almost the same at large scales, whereas a discrepancy in clustering locations is observed at small scales. It is also confirmed that the decreasing trend of the coherence is strongly dependent on the combination of Stokes numbers.

In order to develop a cross spectrum model for estimating the clustering influence on the radar reflectivity factor, we have proposed an exponential model for the wavenumber dependence of the coherence, and introduced the critical wavenumber (i.e., the decay constant for the model) to consider the dependence of the coherence on the Stokes number combination. The coherence data for all combinations of six Stokes numbers ranging from 0.05 to 2.0 reveals that the critical wavenumber is inversely proportional to the Stokes number difference, $|\mathrm{St}_1 - \mathrm{St}_2|$. The proposed coherence model enables us to estimate the cross spectrum for arbitrary combinations of Stokes numbers using the power spectrum model proposed by Matsuda et al. (2014). Comparison of the model estimate with the DNS results for a typical droplet size distribution in cumulus clouds confirms the reliability of the proposed model. The r_p^3-weighted power spectrum estimated by the proposed model shows a good agreement with that obtained by the DNS data, indicating that the proposed model can estimate the clustering influence on the radar reflectivity factor to a sufficient accuracy.

Finally, the proposed model has been applied to high-resolution cloud-simulation data of Onishi and Takahashi (2012). The data were obtained using the Multi-Scale Simulator for the Geoenvironment (MSSG), which is a multi-scale non-hydrostatic atmosphere-ocean coupled model. The cloud and rain droplet size distribution was explicitly calculated at each grid using a spectral-bin cloud microphysics scheme. The result shows that the influence of turbulent clustering can be significant for the near-top of turbulent clouds, where the energy dissipation rate is large and the droplet sizes are small.

Appendix A: Power spectrum model proposed for turbulent clustering of monodisperse droplets

The parameterization for $E^*_\mathrm{np}(\xi|\mathrm{St})$ proposed by Matsuda et al. (2014) is given by

$$E^*_\mathrm{np}(\xi|\mathrm{St}) = \frac{c_1\xi^\alpha}{\left\{1+(c_1/c_2)^{2\gamma/(\alpha-\beta)}\,\xi^{2\gamma}\right\}^{(\alpha-\beta)/2\gamma}}. \qquad \text{(A1)}$$

where c_1, c_2, α, β, and γ are the model parameters given by the functions of St as follows:

$$\begin{cases} c_1 &= 13.4/[1+(\mathrm{St}/0.29)^{-1.25}], \\ c_2 &= 6.7\mathrm{St}^{1.6}/[1+0.68\mathrm{St}^{3.7}], \\ \alpha &= 0.44-0.20\ln\mathrm{St}, \\ \beta &= -1+0.77\mathrm{St}^{-1}\exp\left[-(\ln\mathrm{St}-0.55)^2/2.0\right], \\ \gamma &= 1.6. \end{cases} \qquad \text{(A2)}$$

© Author(s) 2018. CC BY 4.0 License.

Matsuda et al. (2014) confirmed that this parameterization is reliable for $\mathrm{St} \leq 2.0$: in this range, the error of the parameterization is smaller than 1 dB.

Acknowledgements. This research was supported by JSPS KAKENHI Grant Number JP17K14598. The numerical simulations presented were carried out on the Earth Simulator supercomputer system of the Japan Agency for Marine-Earth Science and Technology (JAMSTEC).

© Author(s) 2018. CC BY 4.0 License.

References

Ayala, O., Rosa, B., and Wang, L.-P.: Effects of turbulence on the geometric collision rate of sedimenting droplets. Part 2. Theory and parameterization, New J. Phys., 10, 075 016, 2008a.

Ayala, O., Rosa, B., Wang, L.-P., and Grabowski, W.: Effects of turbulence on the geometric collision rate of sedimenting droplets. Part 1. Results from direct numerical simulation, New J. Phys., 10, 075 015, 2008b.

Bohren, C. and Huffman, D.: Absorption and Scattering of Light by Small Particles, Wiley, 1983.

Bringi, V., Chandrasekar, V., Balakrishnan, N., and Zrnić, D.: An examination of propagation effects in rainfall on radar measurements at microwave frequencies, J. Atmos. Oceanic Technol., 7, 829–840, 1990.

Carey, L., Rutledge, S., Ahijevych, D., and Keenan, T.: Correcting Propagation Effects in C-Band Polarimetric Radar Observations of Tropical Convection Using Differential Propagation Phase, J. Atmos. Sci., 39, 1405–1433, 2000.

Chen, L., Goto, S., and Vassilicos, J.: Turbulent clustering of stagnation points and inertial particles, J. Fluid Mech., 553, 143–154, 2006.

Chun, J., Koch, D., Rani, S., Ahluwalia, A., and Collins, L.: Clustering of aerosol particles in isotropic turbulence, J. Fluid Mech., 536, 219–251, 2005.

Dombrovsky, L. and Zaichik, L.: An effect of turbulent clustering on scattering of microwave radiation by small particles in the atmosphere, J. Quant. Spectro. Rad. Trans., 111, 234–242, 2010.

Erkelens, J., Venema, V., Russchenberg, H., and Ligthart, L.: Coherent Scattering of Microwave by Particles: Evidence from Clouds and Smoke, J. Atmos. Sci., 58, 1091–1102, 2001.

Gossard, E. and Strauch, R.: Radar Observation of Clear Air and Clouds, vol. 14 of *Developments in Atmospheric Science*, Elsevir, New York, 1983.

Hess, M., Koepke, P., and Schult, I.: Optical Properties of Aerosols and Clouds: The Software Package OPAC, Bull. Am. Meteor. Soc., 79, 831–844, 1998.

Hirt, C. and Cook, J.: Calculating three-dimensional flow around structures, J. Comput. Phys., 10, 324–340, 1972.

Knight, C. and Miller, L.: Early radar echoes from small, warm cumulus: Bragg and hydrometeor scattering, J. Atmos. Sci., 55, 2974–2992, 1998.

Kostinski, A. and Jameson, A.: On the spatial distribution of cloud particles, J. Atmos. Sci., 57, 901–915, 2000.

Matsuda, K., Onishi, R., Hirahara, M., Kurose, R., Takahashi, K., and Komori, S.: Influence of microscale turbulent droplet clustering on radar cloud observations, J. Atmos. Sci., 71, 3569–3582, 2014.

Matsuda, K., Onishi, R., and Takahashi, K.: Influence of gravitational settling on turbulent droplet clustering and radar reflectivity factor, Flow Turb. Combust., 98, 327–340, 2017.

Maxey, M.: The gravitational settling of aerosol particles in homogeneous turbulence and random flow fields, J. Fluid Mech., 174, 441–465, 1987.

Morinishi, Y., Lundm, T., Vasilyev, O., and Moin, P.: Fully conservative higher order finite difference schemes for incompressible flow, J. Comput. Phys., 143, 90–124, 1998.

Onishi, R. and Takahashi, K.: A Warm-Bin–Cold-Bulk Cloud Microphysical Model, J. Atmos. Sci., 69, 1474–1497, 2012.

Onishi, R. and Vassilicos, J.: Collision Statistics of Inertial Particles in Two-Dimensional Homogeneous Isotropic Turbulence with an Inverse Cascade, J. Fluid Mech., 745, 279–299, 2014.

© Author(s) 2018. CC BY 4.0 License.

Onishi, R., Takahashi, K., and Komori, S.: Influence of gravity on collisions of monodispersed droplets in homogeneous isotropic turbulence, Phys. Fluids, 21, 125 108, 2009.

Onishi, R., Baba, Y., and Takahashi, K.: Large-Scale Forcing with Less Communication in Finite-Difference Simulations of Steady Isotropic Turbulence, J. Comput. Phys., 230, 4088–4099, 2011.

Pinsky, M., Khain, A., and Krugliak, H.: Collision of Cloud Droplets in a Turbulent Flow. Part V: Application of Detailed Tables of Turbulent Collision Rate Enhancement to Simulation of Droplet Spectra Evolution, J. Atmos. Sci., 65, 357–374, 2008.

Reade, W. and Collins, L.: Effect of preferential concentration on turbulent collision rates, Phys. Fluids, 12, 2530, 2000.

Rogers, R. and Brown, W.: Radar Observations of a Major Industrial Fire, Bull. Amer. Meteor. Soc., 78, 803–814, 1997.

Squires, K. and Eaton, J.: Preferential concentration of particles by turbulence, Phys. Fluids A, 3, 1169–1178, 1991.

Sundaram, S. and Collins, L.: Collision statistics in an isotropic particle-laden turbulent suspension. Part 1. Direct numerical simulations, J. Fluid Mech., 335, 75–109, 1997.

van Zanten, M., Nuijens, L., and Siebesma, A.: Precipitating Shallow Cumulus Case1, http://www.knmi.nl/samenw/rico/.

Wang, L. and Maxey, M.: Settling velocity and concentration distribution of heavy particles in homogeneous isotropic turbulence, J. Fluid Mach., 256, 27–68, 1993.

Wang, L., Rosa, B., Gao, H., He, G., and Jin, G.: Turbulent collision of inertial particles: Point-particle based, hybrid simulations and beyond, Int. J. Multiphase Flow, 35, 854–867, 2009.

Zhou, Y., Wexler, A., and Wang, L.: Modelling turbulent collision of bidisperse inertial particles, J. Fluid Mech., 433, 77–104, 2001.